The Application of Flow360 to the 7th Drag Prediction Workshop Cases

Thomas Fitzgibbon*, CJ Doolittle[†], Philippe Spalart[‡]
Flexcompute Inc, Belmont, Massachusetts, 02138

Qiqi Wang[§]
Flexcompute Inc, Belmont, Massachusetts, 02138
Massachusetts Institute of Technology, Cambridge, Massachusetts 02139

This paper presents the contribution of Flexcompute to the 7th Drag Prediction Workshop, with CFD simulations computed using the Flow360 solver. Three cases were performed, including a grid convergence study, an alpha sweep, and Reynolds number study. The analysis is focused on different RANS closures with comparative predictions performed using the SA, $k - \omega$ SST, SA-QCR and SA-RC-QCR turbulence models. Particular attention is put on the ability of each model to accurately predict the aircraft drag and pitching moment as well as on the prediction of the wing-body juncture and shock-induced separations. Comparisons are made with available experimental data including integrated loads and surface pressure predictions. The SA-RC-QCR model was able to accurately predict the drag magnitude and pitching moment break trends and showed good correlation with experiments for surface pressures.

I. Nomenclature

AR	=	wing aspect ratio
b	=	wing span
C_D	=	total drag coefficient
C_{Dp}	=	pressure drag coefficient
C_{Dv}	=	viscous drag coefficient
C_L	=	lift coefficient
C_M	=	pitching moment coefficient
C_P	=	pressure coefficient
C_{ref}	=	wing reference chord ~ MAC
E	=	elastic modulus
eta	=	wing spanwise location normalized by wing span
HiQ	=	high dynamic pressure conditions
LoQ	=	low dynamic pressure conditions
M	=	Mach number
MRC	=	moment reference center
N	=	number of grid nodes
Q	=	dynamic pressure
Re	=	chord Reynolds number
S_{ref}	=	wing reference area
X/c	=	wing chord fraction
y^+	=	nondimensional wall distance in wall units
α	=	angle of attack
$\Lambda_{c/4}$	=	sweep at quarter chord
λ	=	taper ratio

*CFD Research Scientist, AIAA Senior Member
[†]Director of Applied CFD, AIAA Senior Member
[‡]Head of Fluid Mechanics, AIAA Associate Fellow
[§]Associate Professor, Department of Aeronautics and Astronautics, MIT. Co-founder of Flexcompute, AIAA Associate Fellow

II. Introduction

Drag predictions in transonic flow conditions are considered as a complex problem for CFD codes, due to the presence of shock-induced separation and potential unsteadiness associated with buffet. With increasing angle of attack, the shock-induced separation intensifies, leading to a break in the pitching moment curve and increase in drag, which can have implications on the performance, safety and certification of the aircraft. Accurate predictions of transonic flow physics and drag/moment increments with changes in alpha will therefore, have consequences on the aircraft programme costs and timelines. The drag prediction workshop [1] was formed to assess the capability of modern CFD codes to accurately predict the loads on an aircraft in transonic flow, and help guide developments in CFD codes.

Considerable work has been performed in the past, with the current drag prediction workshop on its 7th edition. The first three workshops focused on the DLR F6 geometry [2], with a grid convergence study and alpha sweep performed, with main issues related to generating a series of consistent grids for a grid convergence study and wing-body juncture separation appearing in a number of solutions. The 4th edition [3] (and following workshops) examined the Common Research Model (CRM), and looked at downwash effects, including simulations with and without the tail. This workshop targeted blind predictions, with no experimental data available for comparison. Due to the large scatter between different participants, the geometry was simplified for the 5th workshop [4] by removing the tail. Optional turbulence model verification cases were also introduced to improve the consistency between different CFD codes. Once again, a grid convergence and alpha sweep study were performed, with offsets from experimental data in the lift and drag predictions attributed to the neglection of aeroelastic effects. At high alphas, some solutions continued to exhibit high wing-body juncture separation. All solutions were simulated using steady RANS methods and it is unknown whether these methods are suitable at these conditions. The 6th workshop [5] considered the wing/body CRM with static aeroelastic effects, leading to better correlation with experiments. A constant offset in the lift and moment curves, however, was still present and was attributed to excessive aft loading on the outboard wing sections. Other differences, were attributed to premature separation at the wing root, with many participants highlighting the need for the Quadratic Constitutive Relation (QCR) correction in the turbulence model for accurate predictions. The 6th workshop continued to use steady-RANS simulations with buffet reported during experiments at 4 degrees. For the first time, grid-adapted solutions were also submitted.

The 7th drag prediction workshop builds on the previous six editions, by performing analyses at more representative flight Reynolds numbers, 20 million for the CRM wing-body. The testcases include a grid convergence study, alpha sweep and a Reynolds number effect study. The current best modelling practices, however, are still uncertain for accurate predictions of transonic flows with shock-induced separation. For RANS-based simulations, many participants rely on differing grids and turbulence models, leading to significant scatter in the workshop submissions. The main aim of the current work is to assess the capability of CFD for accurate predictions in transonic flows and to provide guidelines with the primary focus on comparing different RANS closure models.

A. Flow360 CFD Solver

Flow360 is based on a hardware/software co-design with emerging computing resources leading to unprecedented solver speed and accuracy. The Flow360 solver is a node-centered unstructured grid solver based on a 2nd order finite volume method. The convective fluxes are discretized using the Roe Riemann solver, whereas central differences are used for the viscous fluxes. MUSCL extrapolation is used to achieve higher order accuracy in space. Flow360 includes a number of standard turbulence models including SA-neg, SA-RC, SA-QCR2000, $k - \omega$ SST, and DDES. In the present work we make use of the QCR and RC corrections to examine whether improved solutions are obtained compared to the baseline SA model. The RC correction, multiplies the production term by a rotation function that aims to capture rotation and curvature effects, which typically leads to reduced eddy viscosity in regions with strong rotation such as vortex cores. The QCR correction introduces anisotropy to the turbulent stresses which are not accounted for in the Boussinesq approximation.

III. Geometry, Meshing and Test Conditions

The focus of the current work is the high-speed CRM geometry [6] in a wing-body configuration (without the tail), shown in Figure 1 from the top view. The CRM geometry was developed with the purpose to provide a validation database for CFD codes. The wing geometry has an aspect ratio of 9.0 with a taper ratio of 0.275. The leading edge sweep angle is 35°, with a Yehudi break along the trailing edge at 37% span. The geometric details are presented in Table 1.
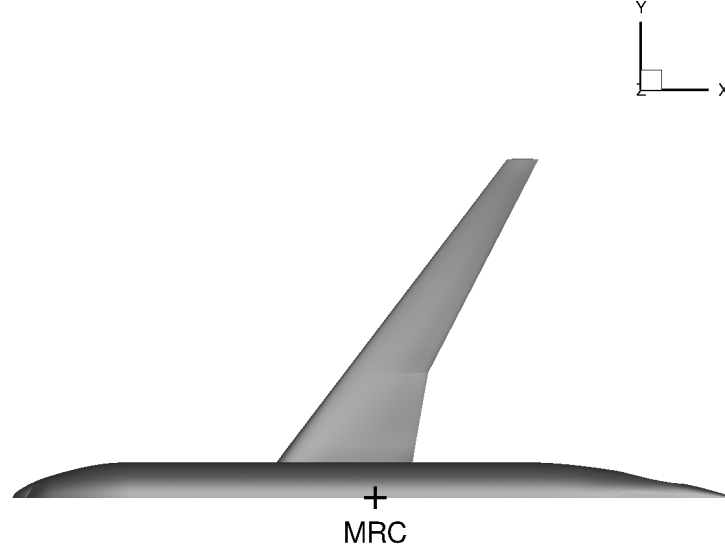
Fig. 1   Geometry of the CRM wing body with the moment center shown.

Table 1   CRM geometric parameters.

Parameter	Value
Reference area, S_{ref}	594,720 in^2
Reference chord, C_{ref}	275.8 in
Span, b	2,313.50 in
Moment reference, $[X_{ref}, Y_{ref}, Z_{ref}]$	[1,325.90 in, 0 in, 177.95 in]
Taper ratio, λ	0.275
Sweep at quarter chord, $\Lambda_{c/4}$	35º
Aspect ratio, AR	9.0

The geometries for the 7th Drag Prediction Workshop included experimental aeroelastic deflections [7] in the geometry at each flow condition measured at the European Transonic Wind Tunnel (in a wing-body-tail configuration). Therefore, the geometry changes both with angle of attack and dynamic pressure (hence the grid also changes). The grids used for the current work were generated by JAXA which are available on the DPW7 website [8]. Four mesh levels were used for the grid convergence study (tiny, coarse, medium, fine), with the medium grid used for the alpha sweep and Reynolds number studies. The grid statistics are presented in Table 2. Visualizations of the surface grid in the root and tip regions are shown in Figure 2 with a slice through the volume grid at the wing mid-span shown in Figure 3 for the tiny and fine grids.

Table 2   Statistics of the JAXA grids used in the current work.

Parameter	Tiny	Coarse	Medium	Fine
Number of nodes	8,698,930	26,891,512	60,184,023	111,843,367
Number of cells	25,294,690	76,058,884	99,985,878	295,240,476
First layer height (non-dim by C_{ref})	8.455E-07	5.638E-07	4.228E-07	3.383E-07
Boundary layer growth rate	1.323	1.205	1.150	1.118

(a) Tiny grid, root region

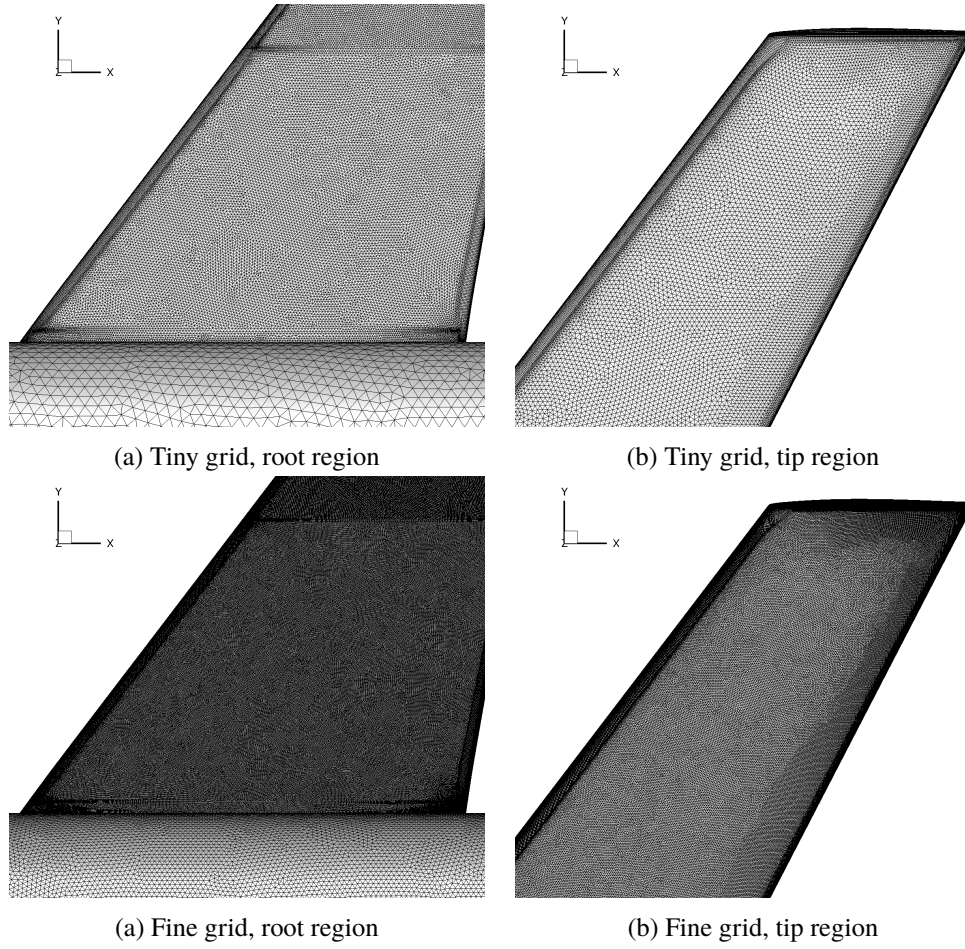(b) Tiny grid, tip region

(a) Fine grid, root region

(b) Fine grid, tip region

Fig. 2 Comparison of the tiny and fine grid surface meshes in the root and tip regions, used for the mesh refinement study.
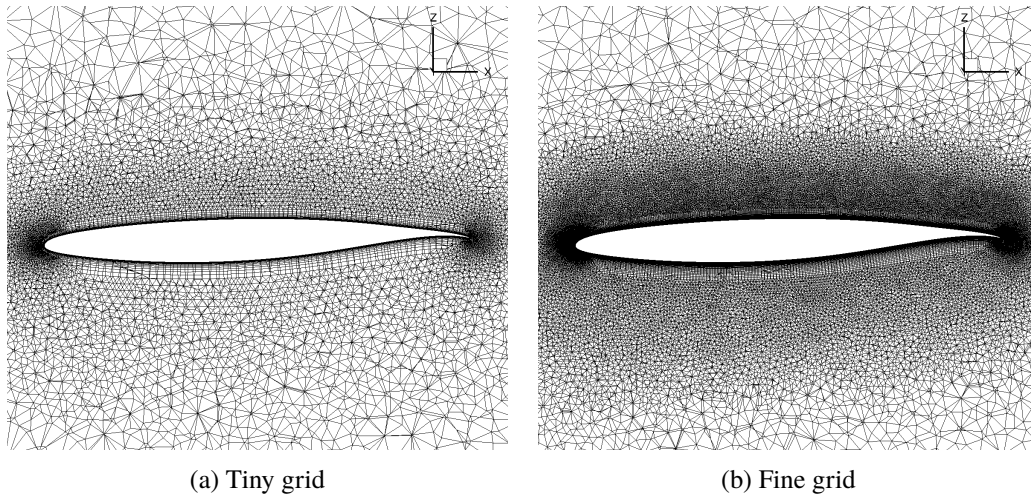

(a) Tiny grid

(b) Fine grid

Fig. 3 Comparison of the tiny and fine grid volume meshes at the mid-span of the wing, used for the mesh refinement study.

The four levels of grids range from 8 to 111 million nodes. As the grid is refined, the first layer height is also reduced, although y^+ is below 1 even for the tiny mesh. The boundary layer growth rate is also reduced. The surface grids involve a number of anisotropic layers from the leading and trailing edges, with isotropy achieved fairly quickly and most of the wing having a uniform mesh spacing. The mesh spacing on the fuselage is significantly larger than on the wing. The spacing on the upper surface is slightly less than found on the lower surface. The same observation can be made by looking at the volume grid slices, comparing the tiny and fine grids, where the fine grid has significantly more refinement on the upper surface in the volume grid. The primary reason for this is the presence of a shock on the upper surface, which must be adequately resolved for accurate integrated load predictions.

The nominal flight conditions are a Mach number of 0.85 at a reference chord-based Reynolds number of 20 million. The first case considers a grid convergence study at $C_L = 0.58$. For this case alpha is adjusted iteratively to obtain the required C_L. User defined dynamics were used to drive alpha, using a proportional integral controller, with a proportional gain of 0.1 and integral gain of 0.001. The case was simulated using the SA and $k - \omega$ SST turbulence models. The second case, examines an alpha sweep in 0.25^o increments from 2.75^o to 4.25^o at the nominal flight conditions, where four turbulence models were used: SA, $k - \omega$ SST, SA-QCR2000, SA-QCR2000-RC. The third case looks at Reynolds number and dynamic pressure (LoQ, Q/E = 0.334 vs HiQ, Q/E = 0.506) effects on the results, with a Reynolds number sweep performed (5 million, 20 million, 30 million) and a single case with increased dynamic pressure. A summary of the testcases performed is shown in Table 3. The CFD simulations were performed in free-air without modelling the wind tunnel. The simulations were run as fully-turbulent without modelling transitional effects. Experimental data is available from the NTF [9] for the integrated loads and surface pressures. However, at a Reynolds number of 20 million only HiQ experimental data [9] is available in the public domain for the wing-body configuration, with LoQ data obtained through the DPW7 workshop committee [10]. The sectional pressure cuts where experimental data is available are shown in Figure 4. Typically, the simulations were ran for 5000 pseudo-steps with the CFL ramped up from 1 to 200 over 2000 iterations (although some simulations converge in 3000 iterations). For cases, where significant separation was seen, an additional 5000 pseudo steps were simulated. The run times for the four meshes simulated using the SA-QCR-RC turbulence model are shown in Table 4, based on the Case 1 simulations. These cases used user defined dynamics to drive alpha to match a given C_L, leading to a minor overhead, hence the Case 2 simulations take slightly less time as the alpha is prescribed.

Table 3   Summary of testcases simulated for the 7th Drag Prediction Workshop.

Case	Flow Conditions	Grids	Turb. Models
Case 1 - Grid Convergence Study	M = 0.85, Re = 20 million, $C_L = 0.58$, Ref. Temp. = -250°F	Tiny, Coarse, Medium, Fine	SA, $k - \omega$ SST
Case 2 - Alpha Sweep Study	M = 0.85, Re = 20 million, Ref. Temp. = -250°F, $C_L = 0.50$ and $\alpha = 2.5^o$ to 4.25^o in 0.25^o increments	Medium	SA, $k - \omega$ SST
Case 3 - Reynolds Number Study	4 cases: Re =5M, LoQ, Ref. Temp. = 100°F Re = 20M, LoQ, Ref. Temp. -250°F Re = 20M, HiQ, Ref. Temp. -182°F Re = 30M, HiQ, Ref. Temp. -250°F	Medium	SA, $k - \omega$ SST

IV. Results

A. Case 1 - Grid Convergence Study

Firstly, the integrated loads convergence with mesh refinement are examined, see Figure 5. For this case, the alpha was adjusted using User Defined Dynamics to achieve a $C_L = 0.58$.

The convergence of the integrated loads with mesh refinement shows very good behavior. Plotted versus grid factor, $N^{-2/3}$, the convergence curves are close to linear, indicating good asymptotic convergence, but not yet converged to a completely grid-independent solution. A minor non-linearity is present in the drag coefficient convergence for the finest
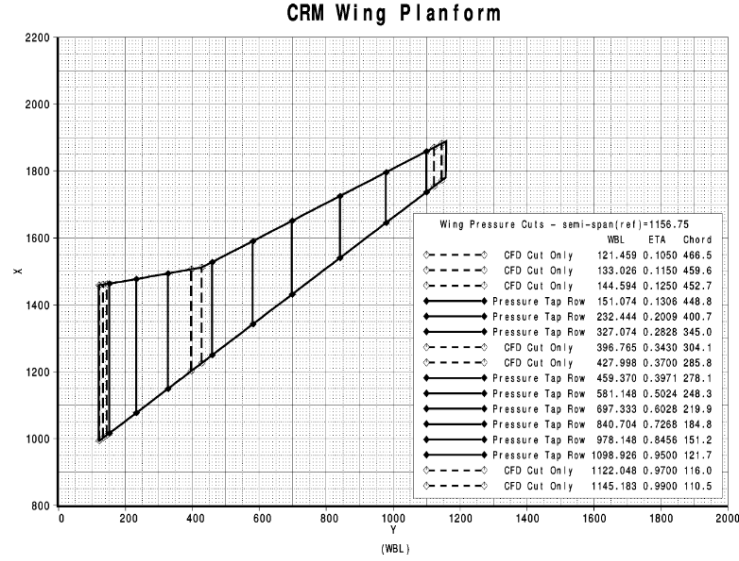
Fig. 4   Geometry of the CRM wing along with locations of the pressure cuts [11].

Table 4   Simulation times based on Case 1 across four different meshes for 5000 psuedo steps with user-defined dynamics.

| Mesh	Number of Nodes	Simulation Time
Tiny	8,698,930	1 min 53 sec
Coarse	26,891,512	4 min 55 sec
Medium	60,184,023	9 min 41 sec
Fine	111,843,367	16 min 40 sec

grid when using the $k - \omega$ SST model which is caused by the viscous component. At a fixed lift coefficient, a finer grid leads to a lower angle of attack, lower drag coefficient and more negative pitching moment. The trends are consistent between the SA and $k - \omega$ SST turbulence models. Comparing the two turbulence models, the SA model leads to a slightly higher angle of attack, higher drag and slightly more negative pitching moment. By separating the drag into pressure and viscous contributions it can be seen that the two turbulence models predict nearly the same pressure drag (with a difference of less than 1 drag count - 0.0001). The main difference comes from the viscous term, where the SA model predicts a higher drag by over 10 drag counts. To analyze where the differences in the integrated loads come from, the surface pressure coefficients were extracted at four spanwise locations, shown in Figure 6.

The surface pressure predictions indicate that near the root at eta = 0.105, the turbulence model sensitivity is greater than the grid level. Firstly, the $k - \omega$ SST results predict a slightly higher stagnation pressure and a further aft shock position. The greatest differences are observed near the trailing edge, where the pressure gradient indicates a larger separation for the SA turbulence model. Further outboard at eta = 0.5024 and 0.7268, the sensitivity between the different results is fairly low. Minor differences exist in the shock position, and hence, gradient of the pressure curve aft of the shock. At the wing tip, the sensitivity is larger, with both grid refinement and turbulence model affecting the shock position. The shock moves aft with grid refinement and is better resolved, showing a sharper pressure discontinuity. The SA turbulence model predicts a further aft shock position, with a stronger shock-induced separation. To analyze these differences in a more qualitative manner, the surface pressure contours were extracted, shown in Figure 7.

The surface pressure isolines, show a main shock inboard that transforms into a lambda shaped shock at the wing tip. With grid refinement, the main shock is much better resolved, as indicated by the greater bunching of the pressure isolines. The lambda shock at the tip is also resolved to a better degree. Minor differences can be seen in the pressure contours ahead of the lambda shock as well as aft, especially when going from the tiny to coarse grid. Comparing the two turbulence models, very little sensitivity can be seen on the pressure contour predictions from a qualitative point of
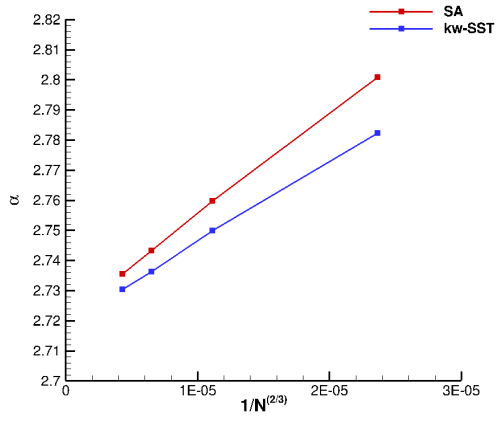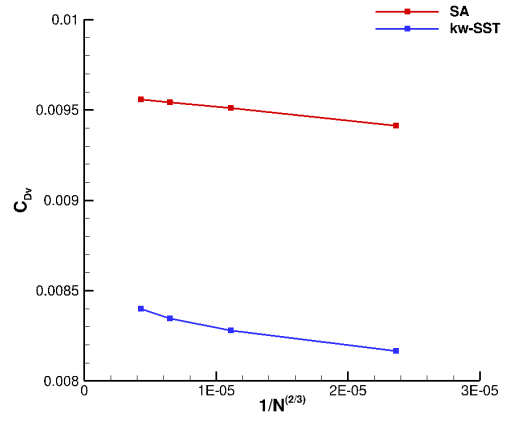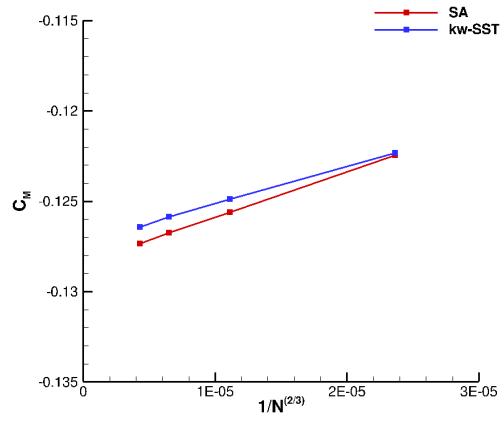
(a)
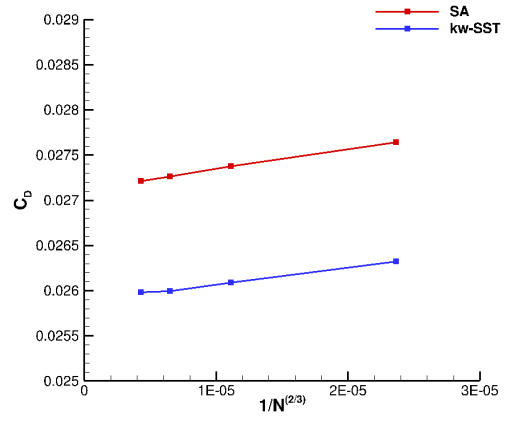
(b)
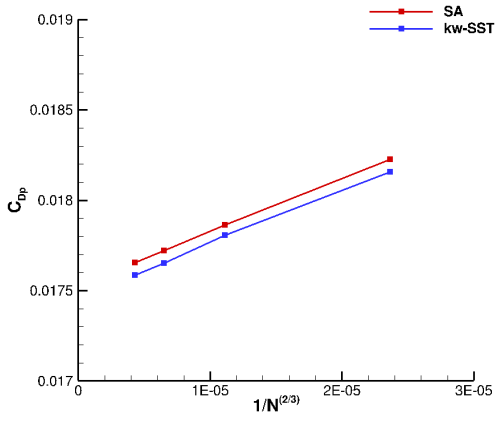
(c)

(d)

e)

Fig. 5   Convergence of integrated loads with mesh refinement, plotted versus grid factor ($N^{-2/3}$ **where N is the number of mesh nodes.**
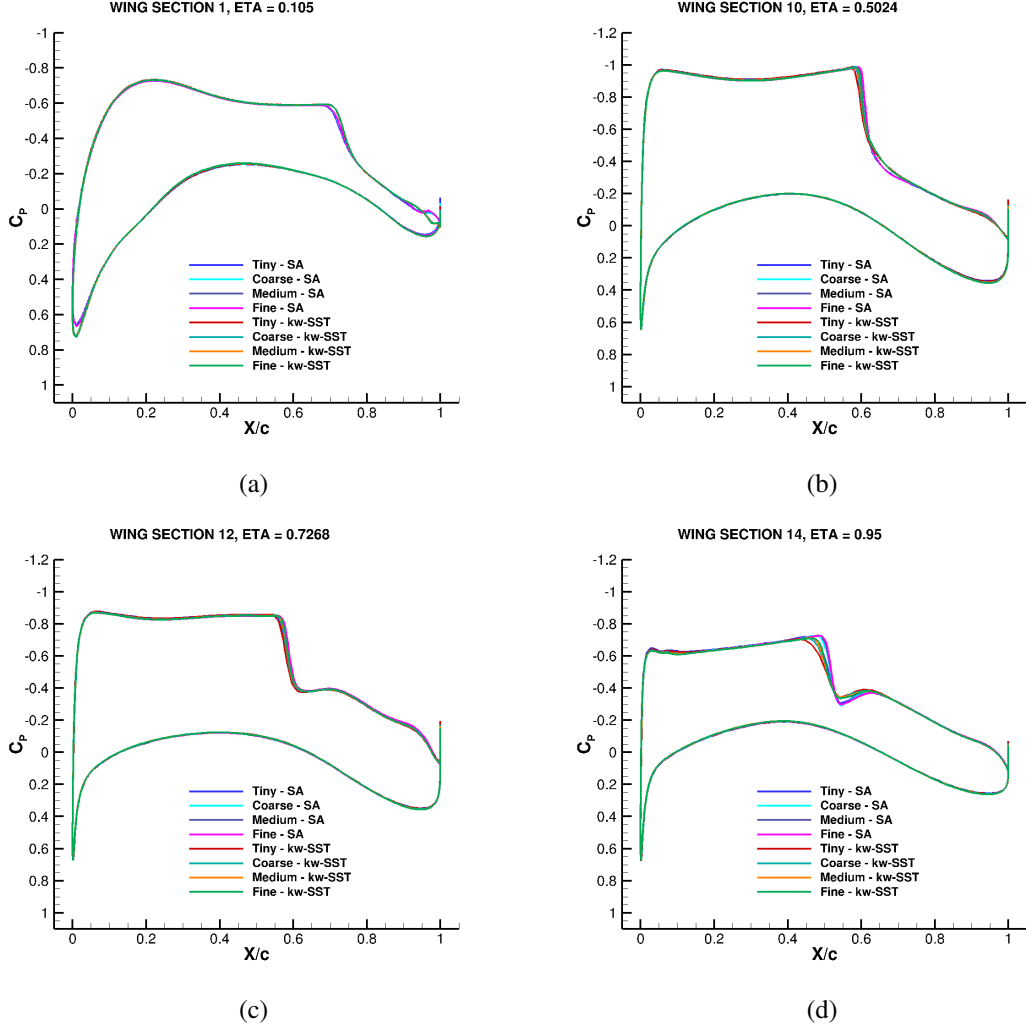
Fig. 6   Comparison of the sectional surface pressure coefficient predictions at four spanwise stations across four grid levels and two turbulence models.

view. The differences in the sectional pressure coefficient predictions are also analyzed further at the root, by visualizing the surface skin friction lines at the wing/fuselage junction, shown in Figure 8.

The wing-body juncture separation patterns, show a low sensitivity to mesh refinement. The recirculation "eyes" on the wing and fuselage do not change greatly in size or position from a qualitative perspective. Greater differences are seen between the two turbulence models. The SA model predicts a much larger wing-body juncture separation in both the spanwise and chordwise directions. The height of the recirculation on the fuselage is similar, but larger in terms of chordwise extent.

B. Case 2 - Alpha Sweep Study

The second case under consideration is the alpha sweep study, which was examined for four different turbulence models. Before presenting the results, some of the differences between the CFD simulation conditions and experimental data must be highlighted. Firstly, the CFD simulations were performed in free-air whereas the experimental data was corrected for the presence of the walls. Secondly, the aeroelastic deflections were taken from the ETW tests in a wing-body-tail configuration and the aeroelastic deflections were found to differ between the NTF and ETW facilites as reported in [12], and may also differ with and without the presence of the tail. Finally, the wind tunnel model was mounted on a support, whereas the CFD simulations were performed in free-air, with the support sensitivities examined
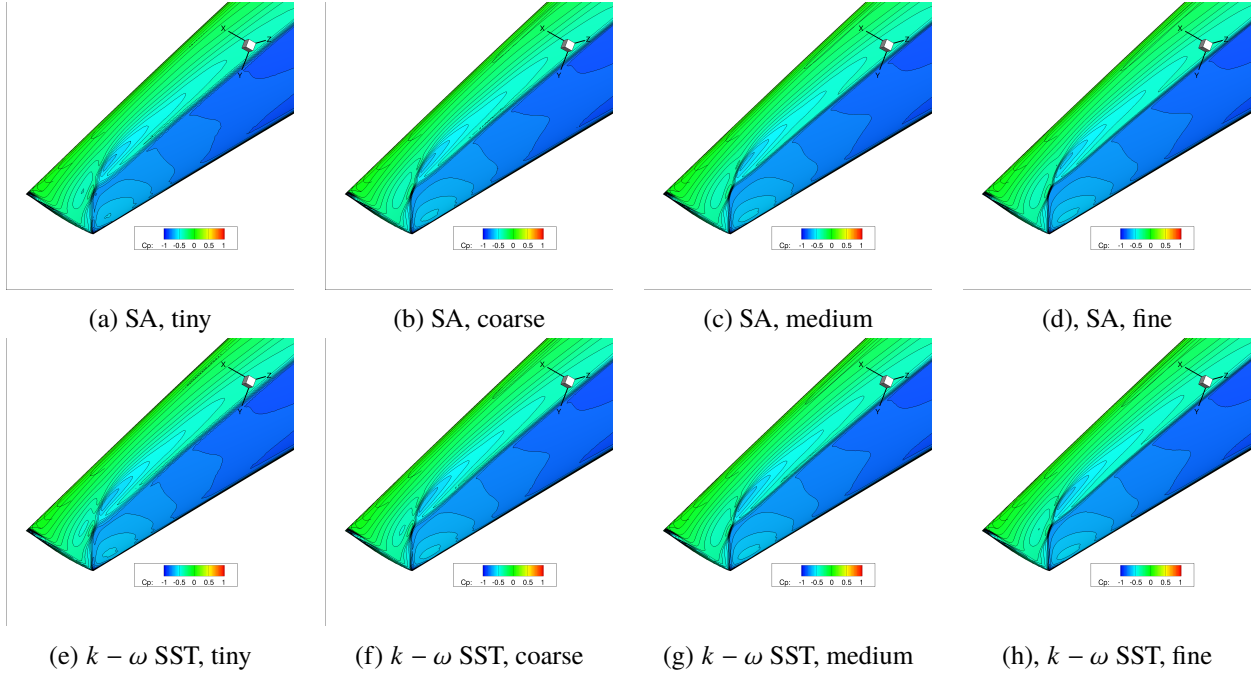
8

Fig. 7 Comparison of the surface pressure contours in the wing tip region across four grid levels and two turbulence models.
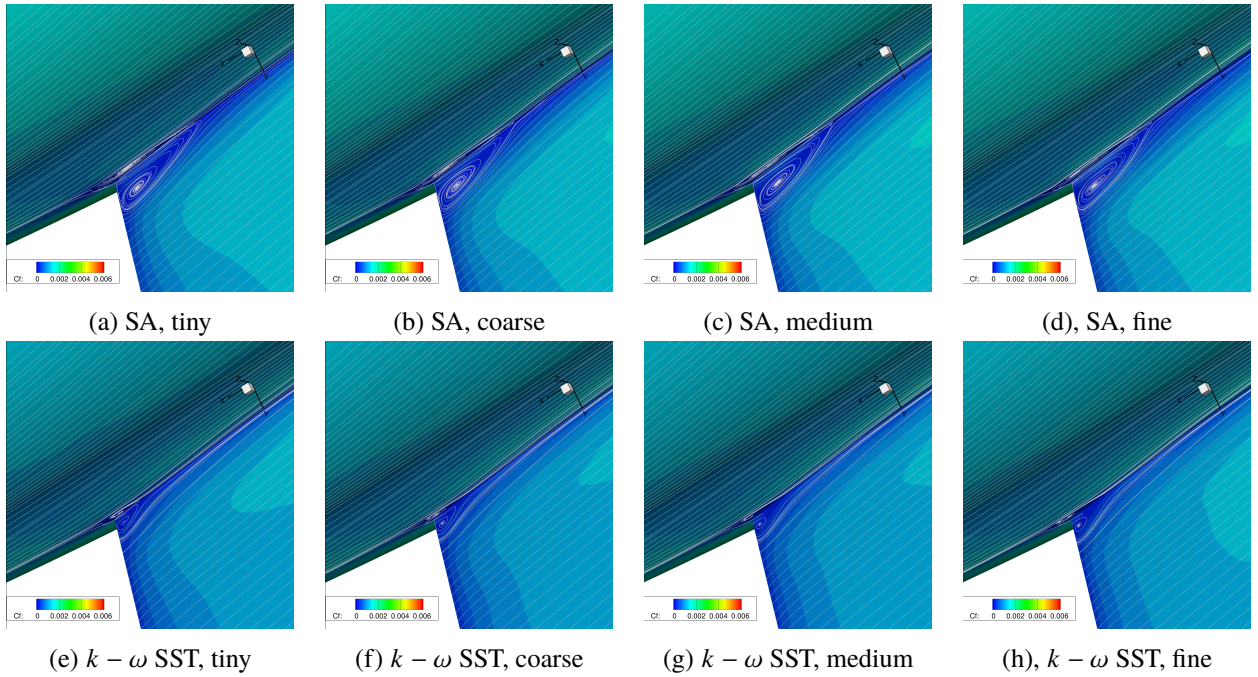

Fig. 8 Comparison of the wing-body juncture separation predictions across four grid levels and two turbulence models.

in [13]. Therefore, some level of discrepancy between CFD simulations and experimental data is to be expected. The integrated loads predictions are shown in Figure 9. The plotted experimental data is from NTF t215r238 and t215r242 [10].
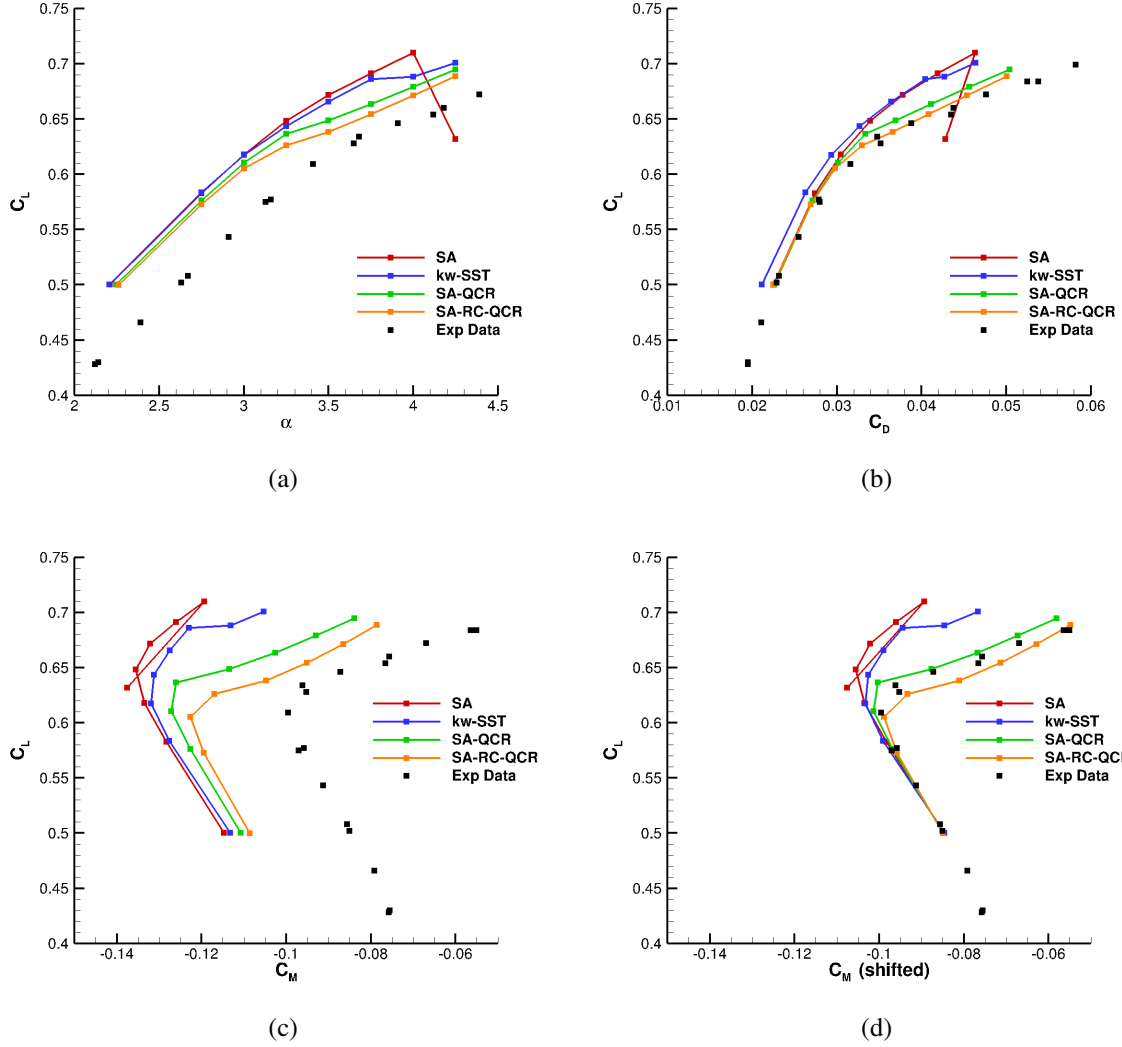
(a)

(b)

(c)

(d)

Fig. 9 Integrated loads predictions for the alpha sweep study on the medium level grid using four different turbulence models.

The lift coefficient curves indicate that at a given angle of attack, the lift is overpredicted compared to experiments, with a fairly constant shift in C_L at low angles of attack. At low angles of attack, the four turbulence models agree very well in terms of lift coefficient, with the SA-RC-QCR and SA-QCR leading to a slightly lower lift than the SA and $k - \omega$ SST turbulence models. As the angle of attack increases, a step change in the lift slope is seen at around 3.5º for the experimental curve. The SA-QCR and SA-QCR-RC predictions accurately predict this change, with a similar lift curve slope as experiments, although at a slightly lower angle attack of around 3.25º. The offset in lift magnitude is also reduced at high angles of attack for the SA-QCR and SA-QCR-RC models. The SA-RC-QCR predictions consistently predict a slightly lower lift than the SA-QCR results at high angles of attack. The SA and $k - \omega$ SST predictions overpredict the lift at high angles of attack, but also do not capture the step change in the lift slope. As the angle of attack increases, the changes in the lift slope are more gradual for these two models, with a larger lift gradient than for the SA-QCR and SA-RC-QCR models and experiments. Furthermore, at the highest angles of attack, significant nonlinearity is seen for the SA and $k - \omega$ SST models, not seen in the experimental data, with the SA predictions indicating a sharp and abrupt stall.

The drag curves show good agreement between the four models at low angles of attack, although the $k - \omega$ SST model predicts a lower drag at a given lift coefficient. As the angle of attack increases, at a given lift coefficient, the SA

10

and $k - \omega$ SST turbulence models predict a lower drag than experiments. Similarly, as with the lift curves, the change in the slope of the drag polar is not well captured. The agreement to experiments for the SA-QCR and SA-RC-QCR models is much better, with an accurate prediction of both the magnitude and trend, especially for the SA-RC-QCR model which predicts a slightly higher drag than the SA-QCR model.

The pitching moment predictions also indicate an overprediction in the magnitude of the negative pitching moment, even with static aeroelastic effects included. Similar observations were found in the previous, 6 [th] Drag Prediction Workshop [5]. To assess the accuracy in terms of the captured trends, especially the pitch moment break, a shift was applied to the curves to align each prediction with the experimental data at low angles of attack (see Figure 9 (d)). After applying the shift, we can see that the SA and $k - \omega$ SST results fail to capture the pitching moment break shape, resulting in a more gradual curve. The SA-QCR and SA-QCR-RC results do very well in capturing the overall trends. The best agreement is obtained with SA-RC-QCR model which predicts a slightly less negative pitching moment than the SA-QCR model for a given C_L at high angles of attack. Based on the integrated loads comparisons, significantly better agreement with experimental data is obtained when using the QCR correction. Further analysis is performed to understand the reasons for integrated loads trends, with the surface pressure predictions examined at four spanwise locations in Figure 10. The plotted experimental pressure data is from NTF t215r159 [9].

At the most inboard station (eta=0.131) at low angles of attack, good agreement with experimental data is obtained for all turbulence models compared to experiments, with the four models showing only a minor sensitivity in the shock position. However, at this location, the reduced suction further upstream is not captured on the current grid. As the angle of attack increases to 4°, the $k - \omega$ SST model indicates separated flow at the trailing edge as the pressure no longer recovers, with the other three models still leading to good correlations and attached flow. At the highest examined angle of attack, the SA model leads to a sharp separation across a large portion of the aerofoil section, with $k - \omega$ SST model showing a similar pressure gradient as at 4°. The SA-QCR and SA-QCR-RC still show fully attached flow with good agreement with experiments. Further outboard at eta = 0.502, the overall agreement with experiment is excellent for all four models, at the lower angles of attack. As the angle of attack increases, a sensitivity to different turbulence models appears in terms of the shock position and aft loading. The SA model appears to be fully attached with a shock that is located the most aft out of the four models, with the SA-RC and SA-QCR-RC models indicating signs of separated flow. At the highest angle of attack of 4.25°, the SA-RC and SA-QCR-RC models lead to the best agreement with experimental data, with the SA model indicating fully-attached flow. At eta = 0.727, greater differences are seen between the four models. At the lowest angle of attack, the shock position is further aft than experiments, with the four models all differing in their predicted position. As the angle of attack increases to 3.5°, the different shock position between models is increased, with SA-RC-QCR and SA-RC predicting a more upstream shock position. The addition of the RC correction appears to move the shock slightly further upstream. At the two highest angles of attack the SA and $k - \omega$ SST models predict a more aft shock position with attached flow at the trailing edge. The SA-QCR and SA-RC-QCR models lead to better agreement in the shock position compared to experiments, but lead to poorer agreement in the surface pressures at the trailing edge, where the experiments indicate flow reattachment past the shock. Another aspect that must be highlighted is a slightly higher loading ahead of the shock than experiments. At the most outboard section (eta=0.95), the loading upstream of the shock is higher than experimental data. This overpredicted outboard loading is seen as the main contributor to the elevated lift coefficient and more negative pitching moment as compared to experimental results. One of the reasons for this behaviour is likely to be due to different aeroelastic deflections used in CFD (from ETW) than during experiments (from NTF). As seen in Figure 1, due to the high sweep of the wing, the outboard sections are behind the moment reference location, hence the entire section loading contributes to a negative pitching moment. Comparing the different turbulence models, similar results are seen at 3°. As the angle of attack increases, the SA-QCR and SA-RC-QCR predict a more upstream shock location than the SA and $k - \omega$ SST turbulence models and follow the experimental pressures past the shock more closely. The differences in the section pressures are analyzed further in a more qualitative manner, with the skin friction lines visualized in Figure 11.

The skin friction lines show a high degree of similarity at 3°, with only minor differences between the four turbulence models in the size of the shock-induced separation near the mid-span of the wing. As the angle of attack increases to 3.5° a greater region of flow reversal is seen with separation from the trailing edge, which is stronger for the SA-QCR and SA-QCR-RC predictions compared to the SA and $k - \omega$ SST results. At 3.5°, the $k - \omega$ SST model predicts the weakest reduction in skin friction. At 4°, the region of separated flow from the trailing edge, increases in size in both the spanwise and chordwise directions. The small wing-body juncture separation also becomes more pronounced with the $k - \omega$ SST model predicting a much larger separation compared to the other three models. At the highest angle of attack, the SA model stalls sharply inboard, with only a very small wing-body juncture separation for the SA-QCR and SA-QCR-RC models. A large region of reversed flow from the trailing edge is seen for these two models at approximately
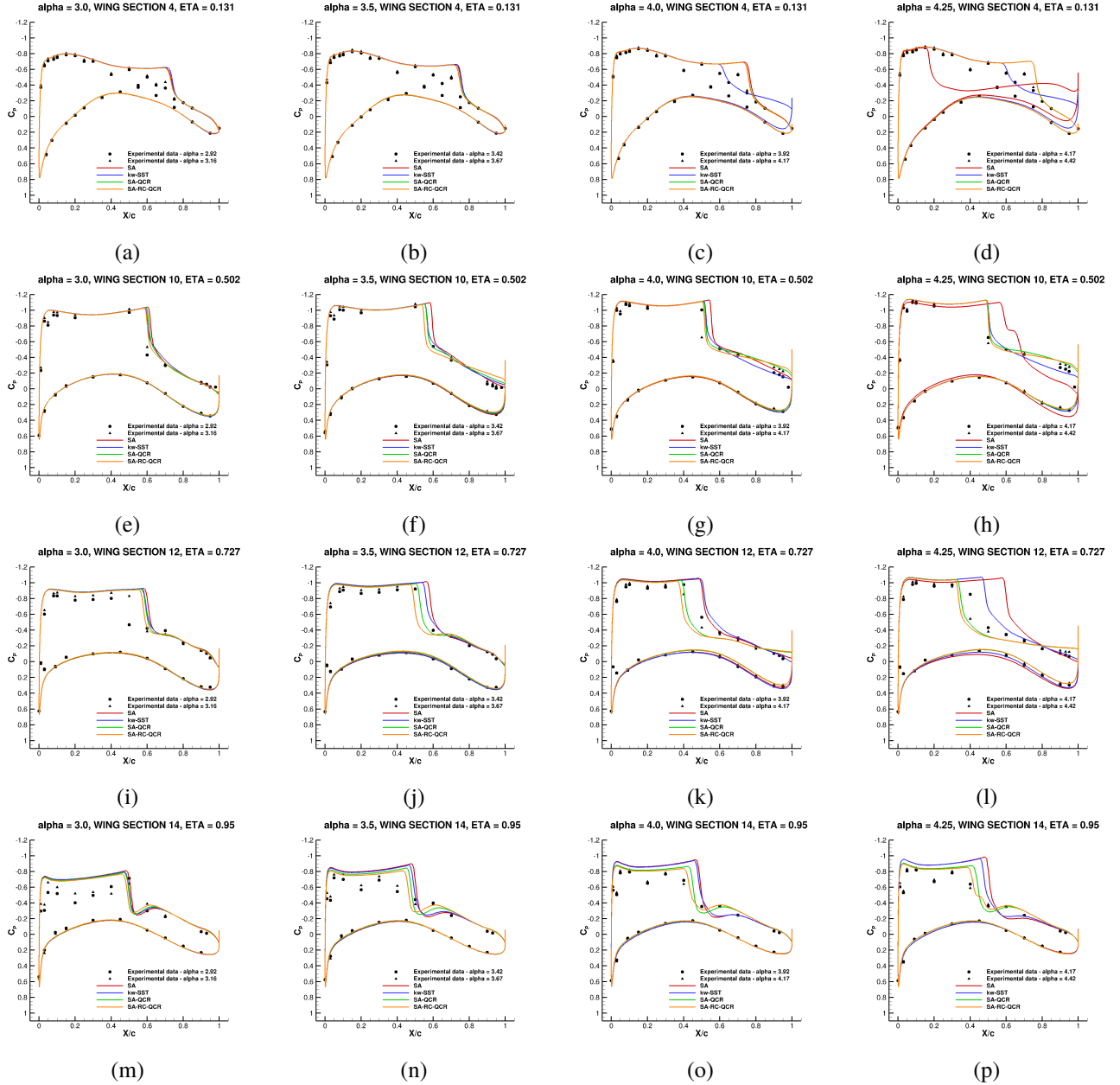
11

Fig. 10 Comparison of the sectional surface pressure coefficient predictions at four spanwise stations and four angles of attack for four different turbulence models with experimental data.

0.75 span, which is not present for the SA prediction. The $k - \omega$ SST model also shows this reverse flow region, but is weaker than for the SA models with corrections. The differences in the wing-body juncture separation are examined in more detail by examining the skin friction lines at the wing-fuselage junction near the trailing edge, shown in Figure 12.

At 3°, the SA turbulence model predicts the largest wing-body juncture separation, which is larger than the other three models in both the chordwise and spanwise directions. The $k - \omega$ SST model wing-body juncture separation is comparable in size, but perhaps stronger than for the SA-QCR and SA-QCR-RC models. As the angle of attack increases to 3.5° the wing-body juncture separations grow slightly in size, especially in the chordwise direction, with similar trends across the four turbulence models. At 4°, the separation for the $k - \omega$ SST model grows significantly, leading to a separation that is larger than captured by the figure. The wing-body juncture separation also grows significantly in the chordwise direction for the SA model. The SA-RC and SA-RC-QCR models still predict a rather
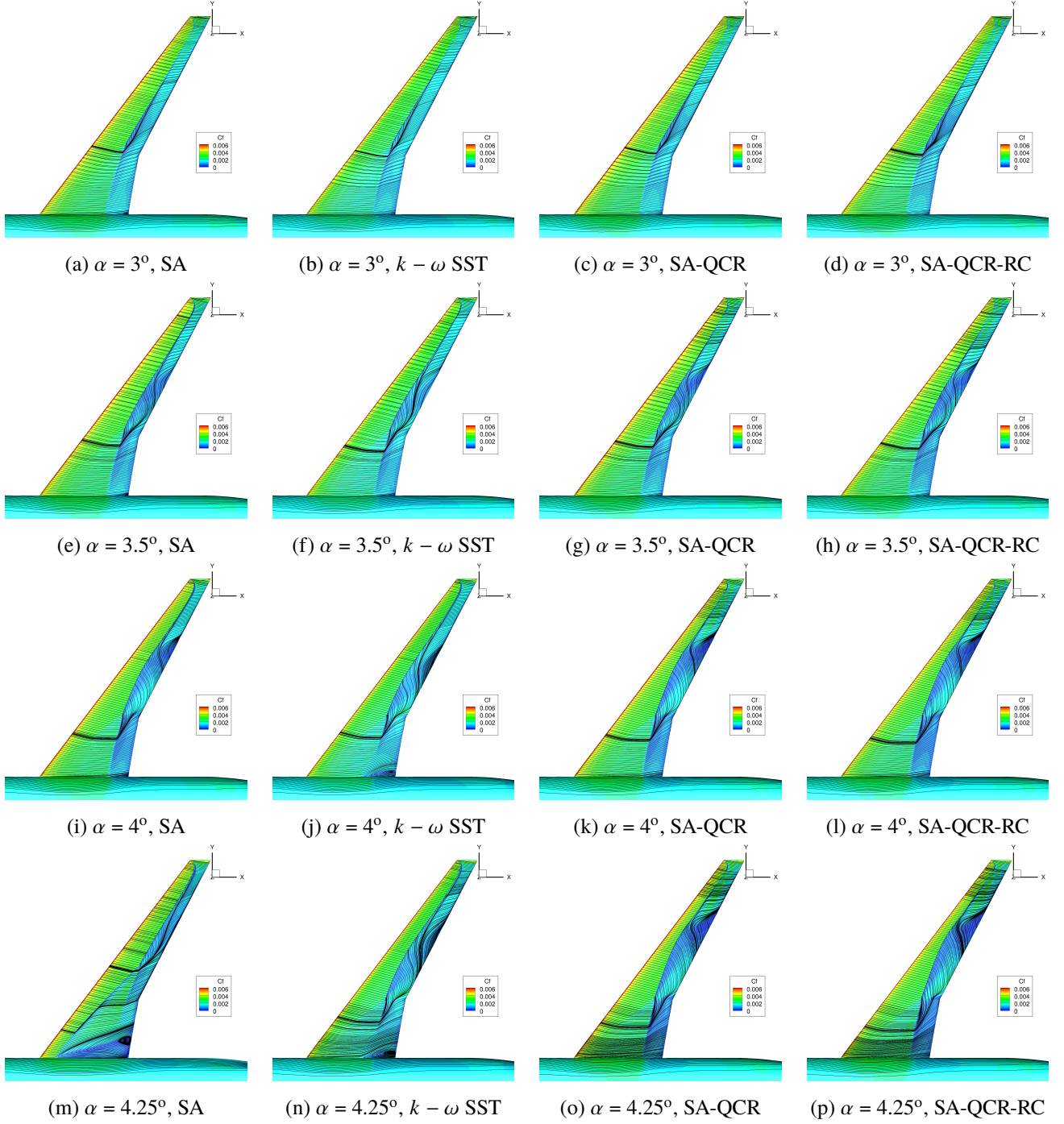
12

(a) $\alpha = 3^o$, SA (b) $\alpha = 3^o$, $k - \omega$ SST (c) $\alpha = 3^o$, SA-QCR (d) $\alpha = 3^o$, SA-QCR-RC

(e) $\alpha = 3.5^o$, SA (f) $\alpha = 3.5^o$, $k - \omega$ SST (g) $\alpha = 3.5^o$, SA-QCR (h) $\alpha = 3.5^o$, SA-QCR-RC

(i) $\alpha = 4^o$, SA (j) $\alpha = 4^o$, $k - \omega$ SST (k) $\alpha = 4^o$, SA-QCR (l) $\alpha = 4^o$, SA-QCR-RC

(m) $\alpha = 4.25^o$, SA (n) $\alpha = 4.25^o$, $k - \omega$ SST (o) $\alpha = 4.25^o$, SA-QCR (p) $\alpha = 4.25^o$, SA-QCR-RC

Fig. 11 Comparison of the skin friction coefficient and skin friction line distributions at four angles of attack across four different turbulence.

small wing-body juncture separation. At the highest angle of attack of 4.25°, a very large separation is seen for the SA model, which is much greater than for the other three turbulence models. The wing-body juncture separation for the $k - \omega$ SST turbulence model does not grow significantly in size compared to the previous angle of attack. The SA-QCR and SA-RC-QCR wing-body juncture separations still remain fairly small. Based on the skin friction lines at the wing-fuselage junction, the QCR correction is crucial for RANS-based models to accurately capture separated flows in junction regions, preventing unphysical large scale separation.
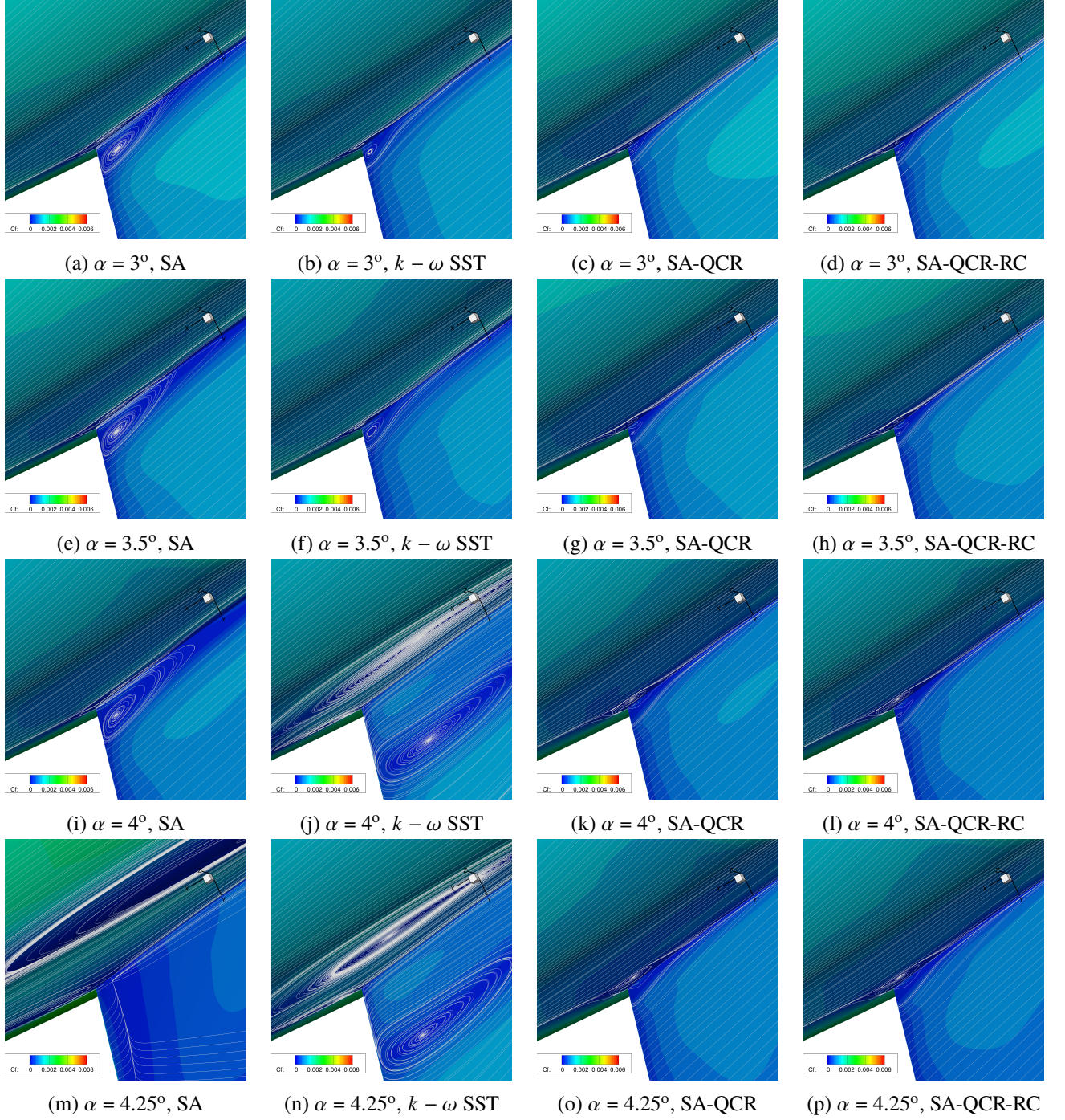
13

(a) $\alpha = 3^o$, SA   (b) $\alpha = 3^o$, $k - \omega$ SST   (c) $\alpha = 3^o$, SA-QCR   (d) $\alpha = 3^o$, SA-QCR-RC

(e) $\alpha = 3.5^o$, SA   (f) $\alpha = 3.5^o$, $k - \omega$ SST   (g) $\alpha = 3.5^o$, SA-QCR   (h) $\alpha = 3.5^o$, SA-QCR-RC

(i) $\alpha = 4^o$, SA   (j) $\alpha = 4^o$, $k - \omega$ SST   (k) $\alpha = 4^o$, SA-QCR   (l) $\alpha = 4^o$, SA-QCR-RC

(m) $\alpha = 4.25^o$, SA   (n) $\alpha = 4.25^o$, $k - \omega$ SST   (o) $\alpha = 4.25^o$, SA-QCR   (p) $\alpha = 4.25^o$, SA-QCR-RC

Fig. 12 Comparison of the wing-body juncture separation predictions at four angles of attack across four different turbulence.

C. Case 3 - Reynolds Number Study

The third case under consideration examines Reynolds number and dynamic pressure effects. Different dynamic pressures at a constant Reynolds number, leads to differences in the static aeroelastic deformation. A comparison of the deflected CRM wing geometries is shown in Figure 13.

The deformed wing geometries have tip deflections of approximately 0.1 C_{ref} and a nose-down elastic twist of approximately 1.1º at LoQ conditions based on [12], although certain differences also exist between facilities (NTF vs
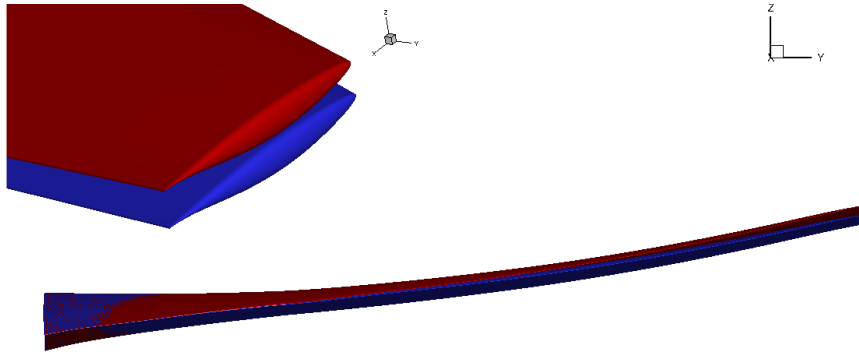
14

Fig. 13   Effect of dynamic pressure on the static wing deformation (LoQ = blue, HiQ = red).

ETW data). Comparing the two dynamic pressure condtions, the HiQ geometry in red to the LoQ geometry in blue, the HiQ geometry has a higher wing bending and elastic twist, due to the larger load on the wing. The impact on the integrated loads along with the effect of Reynolds number for two turbulence models is shown in Figure 14.

Firstly, analysing the effect of Reynolds number, it can be seen that an increase in Reynolds number leads to a reduced alpha for a given lift coefficient ($C_L = 0.5$), reduced drag and larger pitching moment magnitude. These trends are consistent across both turbulence models and both examined dynamic pressures. The reduced drag comes from both the viscous and pressure drag components. The differences in Reynolds number for the LoQ geometry going from 5 million to 20 million are greater than for the HiQ geometry going from 20 million to 30 million, which is attributed to the Reynolds number values themselves rather than the geometry differences.

Comparing the LoQ and HiQ results, it can be seen that the HiQ conditions lead to a higher alpha at a given lift coefficient, slightly higher drag and reduced pitching moment magnitude. This also means that HiQ results would lead to a lower lift coefficient at a given alpha. This can be explained by an increased nose-down twist, which leads to a lower local angle of attack across the span of the wing, hence reduced lift and pitching moment magnitude. Looking at the drag differences in more detail, the minor difference in drag solely comes from the pressure term with negligible differences in the viscous drag values at different dynamic pressures. Comparing the two turbulence models, the differences in predicted lift and and pitching moment are greater at low Reynolds numbers than at higher Reynolds numbers, where consistent results are obtain for both the Spalart-Allmaras and $k - \omega$ SST turbulence models. The drag diffference between the two turbulence models, however, does not seem to change greatly with Reynolds number, and is primarily caused by the viscous drag contribution. The integrated load differences with Reynolds number and dynamic pressure are analysed further by extracting the surface pressure predictions at four spanwise locations, shown in Figure 15.

At the most inboard station, the surface pressure predictions are fairly consistent between the different Reynolds numbers and dynamic pressures. This as expected, as the aeroelastic deformation has a very small impact near the root of the wing. Increasing the Reynolds number, appears to shift the shock aft, with a very minor increase in loading at the trailing edge. Further outboard, at the mid-span, an increase in Reynolds number leads to reduced loading upstream of the shock and increased loading past the shock. Close to no differences are observed with different dynamic pressure at this location. At eta = 0.7268, we start to see the impact of dynamic pressure, with the LoQ results, predicting a higher loading upstream of the shock. Minor differences are also seen in the shock position for the $k - \omega$ SST turbulence model when comparing HiQ vs LoQ results. At the most outboard examined station, once again, an increase in Reynolds number and increase in dynamic pressure reduces the loading on the section. Here, a much larger sensitivity is seen in the pressure gradient ahead of the shock, although the aft loading is farily consistent across multiple Reynolds numbers and dynamic pressure conditions. The skin friction contours were also analysed, and showed an expected result of reduced skin friction at the leading edge of the wing with increasing Reynolds number. The primary takeaway from this case is that, transonic flow predictions are very sensitive to the flow conditions and minor changes in the wing deformation can lead to changes in the intergrated loads.
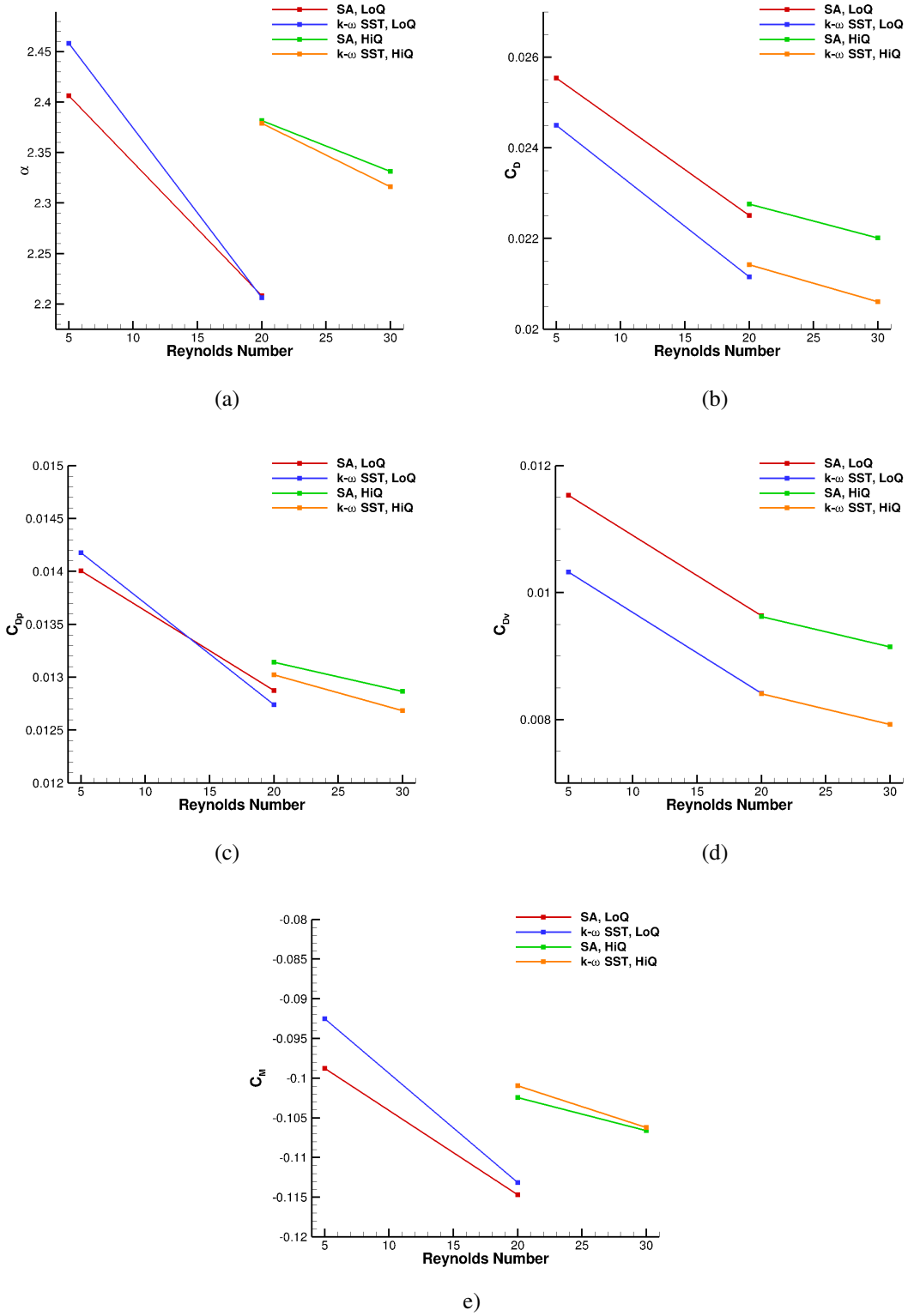
(a)

(b)

(c)

(d)

e)

Fig. 14   Impact of Reynolds number and dynamic pressure on the integrated loads for the Spalart-Allmaras and $k - \omega$ SST turbulence models.
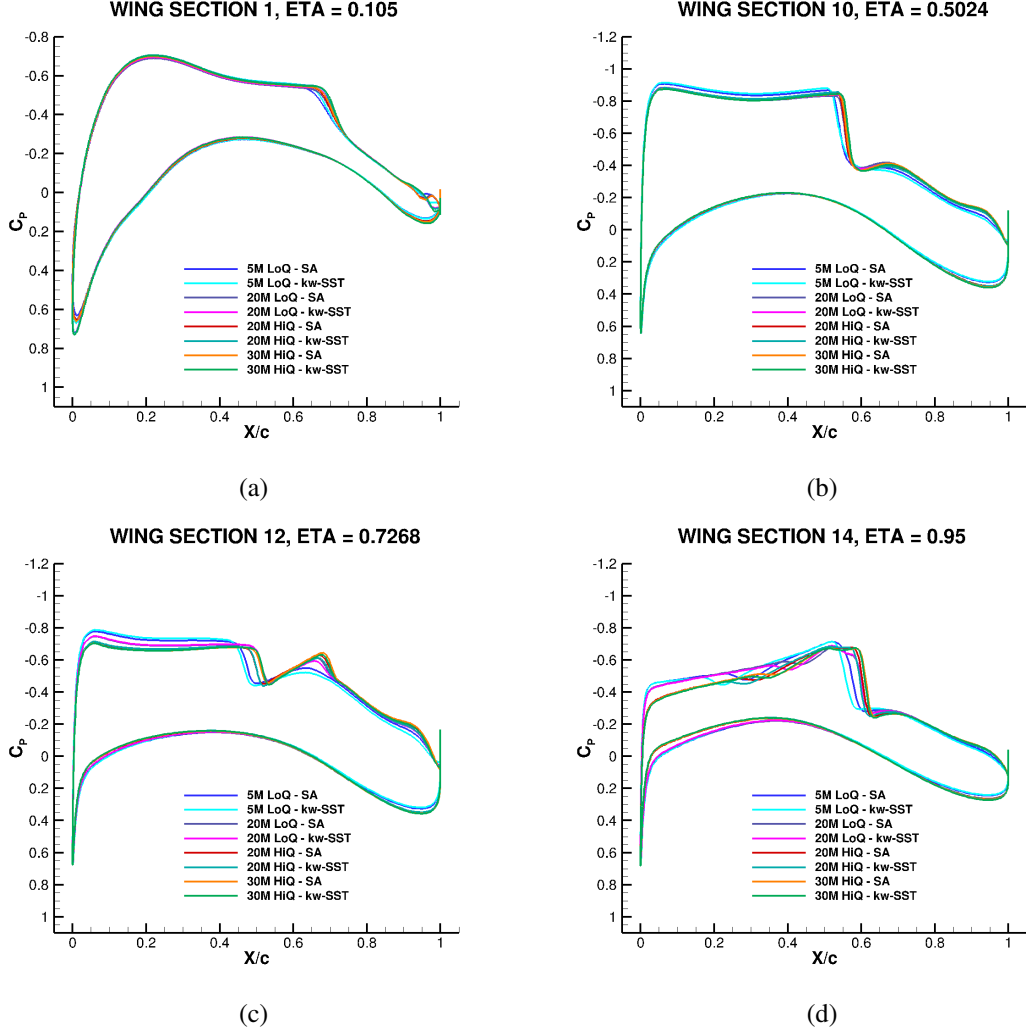
Fig. 15 Comparison of the sectional surface pressure coefficient predictions at four spanwise stations across multiple Reynolds numbers, dynamic pressures and two turbulence models.

V. Conclusions

This work presented the contribution of Flexcompute to the 7th Drag Prediction Workshop. The following conclusions can be made from the current work:

- The grid convergence study showed good convergence properties with the grid refinement primarily affecting the shock position and resolution. The turbulence model primarily affected the viscous drag prediction and size of the wing-body juncture separation.
- The alpha sweep study showed a strong sensitivity of turbulence modeling on the result. The QCR correction was found to significantly improve the correlations with experiments by reducing the unphysical separation at the root. The RC correction was found to also improve results, by shifting the shock forward, reducing the magnitude of the negative pitching moment.
- When using the SA-RC-QCR turbulence model, excellent agreement with experimental data was found in the integrated load trends, with the pitching moment break captured accurately.
- The lift and pitching moment magnitudes were overpredicted at a given alpha due to higher predicted outboard loading compared to experimental data. Similar observations were seen in previous drag prediction workshops, and this issue will be a main topic of future work, which will examine scale-resolving simulations for this configuration.

References

[1] Levy, D., Zickuhr, T., Vassberg, J., Agrawal, S., Wahls, R., Pirzadeh, S., and Hemsch, M., *Summary of Data from the First AIAA CFD Drag Prediction Workshop*, 40th Aerospace Sciences Meeting, Reno, NV, 2002.

[2] Vassberg, J., Tinoco, E., Mani, M., Brodersen, O., Eisfeld, B., Wahls, R., Morrison, J., Zickuhr, T., Laflin, K., and Mavriplis, D., *Summary of Data from the Third AIAA CFD Drag Prediction Workshop*, 45th Aerospace Sciences Meeting, Reno, NV, 2007.

[3] Vassberg, J., Tinoco, E., Mani, M., , Rider, B., Zickuhr, T., Levy, D., Brodersen, O., Eisfeld, B., Crippa, S., Wahls, R., Morrison, J., Mavriplis, D., and Murayama, M., *Summary of Data from the Fourth AIAA CFD Drag Prediction Workshop*, 28th AIAA Applied Aerodynamics Conference, Chicago, IL, 2010.

[4] Levy, D., Laflin, K., Tinoco, E., Vassberg, J., Mani, M., , Rider, B., Rumsey, C., Wahls, R., Morrison, J., Brodersen, O., Crippa, S., Mavriplis, D., and Murayama, M., *Summary of Data from the Fifth AIAA CFD Drag Prediction Workshop*, 51st AIAA Aerospace Sciences Meeting including the New Horizons Forum and Aerospace Exposition, Grapevine, TX, 2013.

[5] Tinoco, E., Brodersen, O., Keye, S., Laflin, K., Feltrop, E., Vassberg, J., Mani, M., Rider, B., Wahls, R., Morrison, J., Hue, D., Roy, C., Mavriplis, D., and Murayama, M., "Summary of Data from the Sixth AIAA CFD Drag Prediction Workshop: CRM Cases," *Journal of Aircraft*, Vol. 55, No. 4, 2018.

[6] Vassberg, J., Dehaan, M., Rivers, M., and Wahls, R., *Development of a Common Research Model for Applied CFD Validation Studies*, 26th AIAA Applied Aerodyanmics Conference, Honolulu, HI, 2008.

[7] European Strategic Wind Tunnels Improved Research Potential (ESWIRP), "The ESWIRP ETW TNA test results," `https://w3.onera.fr/ESWIRP-TNA-ETW-CRM-2014/`, 2014. [Retrieved: 2023-05-03].

[8] Y. Ito and M. Murayama, "Computational Grids - Downloads Page - JAXA," `https://dpw.larc.nasa.gov/DPW7/JAXA_Grids.REV00/`, 2022. [Retrieved: 2023-05-03].

[9] NASA, "NASA Common Research Model - National Transonic Facility Results," `https://commonresearchmodel.larc.nasa.gov/experimental-data/ntf-experimental-results/`, 2019. [Retrieved: 2023-05-03].

[10] DPW7 Committee, "NTF215 Experimental Data," Private Communication, 2023.

[11] DPW7 Committee, "DPW-7 Data Submittal Forms and Postprocessing Information - Wing Section Cut Locations," `https://aiaa-dpw.larc.nasa.gov/Workshop7/forms/DPW_PostProcessing.htm`, 2022. [Retrieved: 2023-05-03].

[12] Rivers, M., Quest, J., and Rudnik, R., *Comparison of the NASA Common Research Model European Transonic Wind Tunnel Test Data to NASA Test Data (Invited)*, 53rd AIAA Aerospace Sciences Meeting, Kissimmee, FL, 2015.

[13] Rivers, M., and Hunter, C., *Support System Effects on the NASA Common Research Model*, 50th AIAA Aerospace Sciences Meeting including the New Horizons Forum and Aerospace Exposition, Nashville, TN, 2012.